Martensitic Transformation in $Fe_xMn_{80-x}Co_{10}Cr_{10}$ High-Entropy Alloy

P. Singh,[1,*] S. Picak,[2,3] A. Sharma,[4,1] Y. I. Chumlyakov,[5] R. Arroyave,[2,3] I. Karaman,[2,3] and Duane D. Johnson[1,6,†]

[1]*Ames Laboratory, U.S. Department of Energy, Iowa State University, Ames, Iowa 50011, USA*
[2]*Department of Mechanical Engineering, Texas A&M University, College Station, Texas 77843, USA*
[3]*Department of Materials Science and Engineering, Texas A&M University, College Station, Texas 77843, USA*
[4]*Sandvik Coromant R&D, Stockholm 12679, Sweden*
[5]*Tomsk State University, Siberian Physical Technical Institute, Novosobornay Square 1, 634050 Tomsk, Russia*
[6]*Department of Materials Science and Engineering, Iowa State University, Ames, Iowa 50011, USA*

(Received 16 May 2021; revised 25 June 2021; accepted 3 August 2021; published 10 September 2021)

High-entropy alloys and even medium-entropy alloys are an intriguing class of materials in that structure and property relations can be controlled via alloying and chemical disorder over wide ranges in the composition space. Employing density-functional theory combined with the coherent-potential approximation to average over all chemical configurations, we tune free energies between face-centered-cubic and hexagonal-close-packed phases in $Fe_xMn_{80-x}Co_{10}Cr_{10}$ systems. Within Fe-Mn-based alloys, we show that the martensitic transformation and chemical short-range order directly correlate with the face-centered-cubic and hexagonal-close-packed energy difference and stacking-fault energies, which are in quantitative agreement with recent observation of two phase region (face-centered cubic and hexagonal closed pack) in a polycrystalline high-entropy alloy sample at $x = 40$ at.%. Our predictions are further confirmed by single-crystal measurements on a $x = 40$ at.% using transmission-electron microscopy, selective-area diffraction, and electron-backscattered-diffraction mapping. The results herein offer an understanding of transformation-induced or twinning-induced plasticity in this class of high-entropy alloys and a design guide for controlling the physics at the electronic level.

DOI: 10.1103/PhysRevLett.127.115704

High-entropy alloys (HEAs) [1–3] and medium-entropy alloys (MEAs) are new, exciting classes of materials with vast design space and emerging unique properties [4–8]. Originally, single-phase, solid-solution formation in HEAs was thought to originate through entropy maximization [1], but recent evidence [9–12] suggests that the entropic description is oversimplified as HEAs and MEAs may display significant local chemical short-range order [13–16]. Outside the HEA space, high-Mn (15–30 at.%) austenitic [γ-face-centered-cubic (γ-fcc) phase] ferrous alloys are a material class that receives special attention due to their low or medium stacking-fault energies (SFEs) [17,18], high ultimate tensile strength (> 1000 MPa) with total elongation over 60% at RT [19], and uses in the automotive industry [20]. A number of studies were performed to tune SFEs in the austenitic alloys to achieve better control over governing deformation mechanisms, e.g., dislocation slip (≥ 40 mJ/m^2), mechanical twinning ($20 - 40$ mJ/m^2), twinning-induced plasticity, and/or martensitic transformation (≤ 20 mJ/m^2), including those in HEAs [21–24]. As expected, the deformation at the low-SFE regime in austenitic (γ-fcc) alloys is mainly realized through a martensitic [ϵ-hexagonal-close-packed (ϵ-hcp)] transformation [25]. The fcc-based, single-phase multi-principal-element solid solutions have gained attention due to their outstanding ductility. However, lower strength limits their use in engineering applications [26,27]. Recent work has shown that a martensitic transformation [5,28,29] or precipitation strengthening [30,31] could provide an effective way to address the strength-ductility trade-off in this important materials class.

Here, we employed density-functional theory (DFT) methods to understand how to tune some of these key properties via alloying and disorder, in particular, the formation-energy (E_{form}), SFE, and short-range order (SRO) of fcc-based solid solutions; see the Supplemental Material [32] for details on methods. We show that chemistry profoundly alters the E_{form} and SFE of $Fe_xMn_{80-x}Co_{10}Cr_{10}$ and can suppress SRO and, hence, long-range order. The DFT calculated E_{form} and SFE, together with experimental observations, reveal details of the strain-driven martensitic (fcc $\rightarrow$ hcp) transformation at $x = 40$ at.%Fe. Our DFT-predicted SRO [13] on the $x = 40$ at.%Fe system indicates a very weak chemical SRO and, hence, very low-temperature ordering behavior (below 50 K). The predicted low-temperature ordering suggests the preference for forming martensite rather than long-range order. MD simulations [54] on this system at RT also show a strain-driven martensitic transformation at 40 at.% Fe. The results reveal a key underpinning of physical principles behind the formation of

martensite and an opportunity for more intelligent design of high-performance HEAs [55] for a more directed exploration of higher-dimensional composition space [6].

Following Hume-Rothery, the phases stability of HEA and MEA systems in different lattice structures can be estimated empirically using valence-electron count (VEC), e.g., bcc (e.g., A2 or Laves phase) for VEC < 7, coexistence of bcc and fcc at $7 <$ VEC < 87, and fcc for VEC > 8 [6]. The solute and host with similar VEC show large solubility, i.e., a metal dissolve of higher valency to a greater extent or lower valency to a lesser extent. These critical values can be directly and more reliably evaluated using DFT [56]. Notably, Mn-based fcc alloys are known for lower VEC than empirically defined solid-solution phase limits; the exceptions are already noted in [56,57]. As such, DFT calculations were performed on $Fe_xMn_{80-x}Co_{10}Cr_{10}$ to avoid the limitations of empirical rules and to detail the thermodynamic stability and planar faults versus x (Fe) (Fig. 1).

Phase stability [Fig. 1(a)] shows a critical range of 40–55 at.%Fe with a possible two-phase region at the crossover in the stability of the fcc and hcp phases, with fcc energetically favorable at low %Fe. The dual-phase alloy in the Fe-rich region can benefit from solid-solution strengthening owing to the decreased SFE [5,58]. The SFE for $Fe_xMn_{80-x}Co_{10}Cr_{10}$ [Fig. 1(b)] first increases with %Fe additions and then shows a precipitous drop within the dual-phase region from 30–50 at.%Fe. The low SFE indicates that an fcc lattice for this system becomes unstable with respect to the formation of intrinsic stacking faults. These results correlate well with the Fe-Mn phase diagram that shows ϵ martensite is not formed above 50 at.% Fe and a higher Mn concentration drives an austenite-only structure [59]. In a pioneering work, Kelly investigated Fe-Ni and Fe-Ni-C alloys with relatively high SFEs [60] and showed that alloys with appreciable Cr or Mn have a low SFE and form martensites associated with planar stacking faults or the formation of "hcp" martensite [61,62].

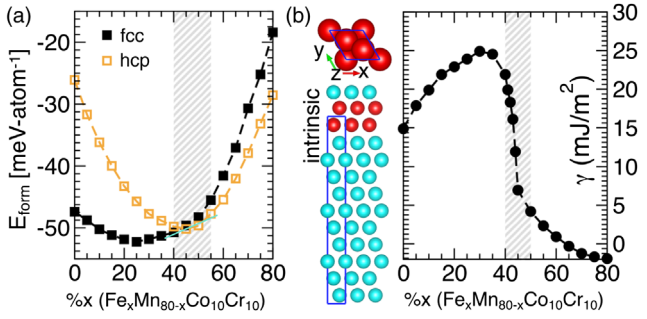

FIG. 1. For $Fe_xMn_{80-x}Co_{10}Cr_{10}$ ($x = 0$–80%), (a) formation energy (E_{form} in meV-atom^{-1}) (see Fig. S1 in the Supplemental Material [32] for volume) vs x, and (b) intrinsic SFE (mJ/m^2) plus a schematic of stacking sequence and outlined unit cell (11 sites). In (a), the dual-phase (fcc + hcp) region is shaded, where SFE (b) drops rapidly with increasing %Fe.

Typically, a medium or negative SFE has been regarded as the crucial indicator of transformation-induced plasticity (TRIP) phenomena [63–69], suggesting a low-energy barrier for fcc-to-hcp transformation [70]. Conventional steels are known for martensitic transitions at medium SFEs, e.g., Fe-Mn-based alloys with SFEs below $11 - 19$ mJ/m^2 and Co-Ni-Cr-Mo alloys below $9 - 15$ mJ/m^2 [71]. This has also been exemplified for Cu-Al [72], Ni-Cu [73], Ni-Fe [73], Ni-Co [74], Co-Ni-Cr-Mo [74], and Fe-Mn-based (twinning-induced plasticity or TRIP steel) alloys [19,58]. However, the difficulty in measuring SFE [17,63–65] makes comparison with theory harder. In Table I, we tabulated calculated SFEs for $Fe_xMn_{80-x}Co_{10}Cr_{10}$ with a comparison to experiments [8] and other Fe-Mn-based alloys [58,75,76]. Our calculations indicate medium-to-low intrinsic SFEs for $Fe_xMn_{80-x}Co_{10}Cr_{10}$ with increasing %Fe. Extrinsic and twinning stacking-fault energies (see Fig. S2 in the Supplemental Material [32]) suggest intrinsic faults are energetically more favorable, i.e., intrinsic stacking-fault energy (ISFE) $<$ extrinsic stacking-fault energy $<$ twinning stacking-fault energy. In Fig. 1(b), the ISFE is nonmonotonic versus x, where the energy needed to alter the fcc stacking sequence [77] is varying dramatically and goes negative with at.%Fe with composition. The dramatic change in the ISFE can be attributed to the relatively large increase in hcp volume compared to fcc (see red zone in Fe-rich region in Fig. S1 of the Supplemental Material [32]). The negative ISFEs in fcc configurations suggest that the hcp stacking would be preferred energetically. Extrinsic stacking-fault energies [see Fig. S2(d) in the Supplemental Material [32]] follow a similar trend as the ISFEs, but unlike the ISFEs they remain positive in the Fe-rich region. No such composition dependence versus %Fe was observed in twinning stacking-fault energies [see Fig. S2(d) in the Supplemental Material [32]].

The phase stability analysis of $Fe_xMn_{80-x}Co_{10}Cr_{10}$ in Fig. 1(a) shows a dual-phase region with onset at 40 at.% Fe. Recently, the $x = 50$ at.%Fe alloy has been reported as

TABLE I. For $Fe_xMn_{80-x}Co_{10}Cr_{10}$, DFT-calculated SFE at 0 K with comparison to experiments [8] at 300 K and Fe-Mn-based alloys [17,58,75,76].

Fe-Mn-based		$Fe_xMn_{80-x}Co_{10}Cr_{10}$ SFE [mJ/m^2]		
Systems	SFE	%x	Theory	Expt
$Fe_{66}Mn_{28}Al_3Si_3$	38.8 ± 5	0	14.7	⋯
$Fe_{69}Mn_{25}Al_3Si_3$	21.0 ± 3	10	19.8	⋯
$Fe_{72}Mn_{22}Al_3Si_3$	15.0 ± 3	20	21.9	⋯
$Fe_{75}Mn_{25}$	27.5 ± 3.3	40	22.3	17 ± 4
$Fe_{78}Mn_{22}$	15.0 ± 1.8	45	7.3	⋯
$Fe_{80}Mn_{20}$	18.0 ± 2.2	60	1.1	⋯
$Fe_{82}Mn_{18}$	22.0 ± 2.6	70	−1.3	⋯
$Fe_{84}Mn_{16}$	26.0 ± 3.1	80	−1.9	⋯

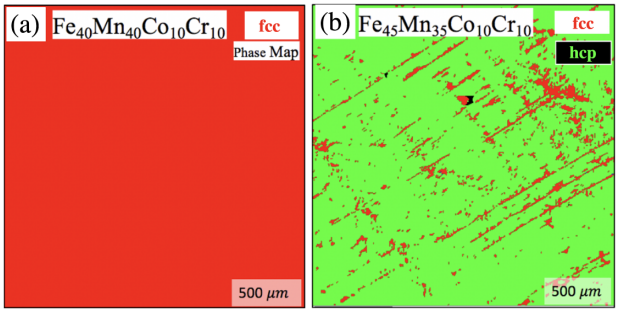

FIG. 2. Electron backscatter diffraction phase maps of (a) 40 at.%Fe, and (b) 45 at.%Fe alloys show single-phase (fcc) and dual-phase (fcc + hcp) microstructures, respectively.

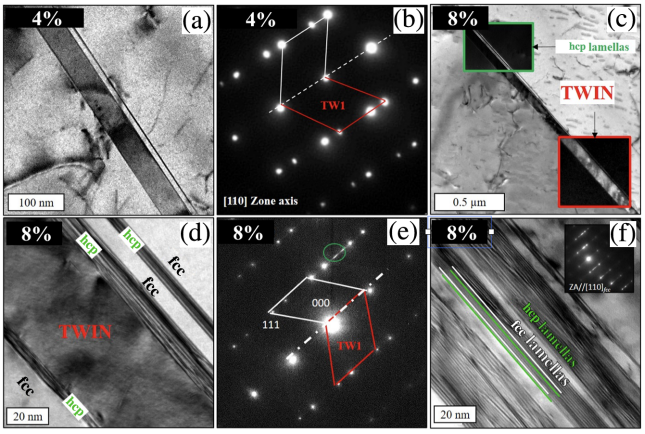

FIG. 3. Bright-field and dark-field TEM micrographs and SADP of [111]-oriented single-crystal with $x = 40$ at.% exhibiting ϵ-martensitic transformation and twin nucleation. (a) Nanotwins at 4% strain, and (b) corresponding SADP. (c) Nucleation of ϵ martensite at the twin boundary at 8% strain (inset: dark-field images confirm this). (d) Higher magnification of (c) and (e) corresponding SADP. (f) Nano ϵ-martensite and fcc bundles.

a two-phase (fcc + hcp) alloy at RT [5], whereas the $x = 40$ at.%Fe alloy is a single-phase fcc at RT [8]. DFT results (Fig. 1) show small $\Delta E_{\text{form}}^{\text{fcc-hcp}}$ for 40 and 45 at.%Fe, with a higher SFE for 40 at.%Fe (22.2 mJ/m^2) compared to 45 at.%Fe (7.3 mJ/m^2). Thus, the higher SFE of fcc 40 at.%Fe alloy plays a key role in stabilizing the single-phase fcc; that is, RT cannot provide enough thermal energy to drive the martensitic transformation in contrast to 45 at.%Fe. To prove our claim, we grew a 40 and a 45 at.%Fe single-crystal HEA (see the experimental methods in the Supplemental Material [32]). Electron backscatter diffraction micrographs [Figs. 2(a) and 2(b)] show single-phase (fcc) and dual-phase (fcc + hcp) microstructures, respectively, for 40 and 45 at.%Fe.

With proper configurational averaging for general HEAs (using the coherent-potential approximation, not just one representative configuration), theory provides a reliable and quantitative prediction of $\Delta E_{\text{form}}^{\text{fcc-hcp}}(x)$ and $\gamma_{\text{SFE}}(x)$ and its dramatic composition dependence, here for $Fe_xMn_{80-x}Co_{10}Cr_{10}$. The small $\Delta E_{\text{form}}^{\text{fcc-hcp}}$ and medium SFE at 40 at.%Fe provide crucial theory guidance for the microstructural evolution in HEA steels.

To confirm, we examined 40 at.%Fe single crystals under RT uniaxial tensile loading. The bright-field TEM micrographs and selective-area diffraction patterns (SADP) are shown in Fig. 3 (also see Fig. S5 in the Supplemental Material [32]). At 4% strain, nanotwin formation was observed in Fig. 3(a) at the beginning of deformation, which is confirmed by SADP in Fig. 3(b). With further increase in strain, ϵ martensite was activated at strains as low as 8% at twin boundaries in Fig. 3(c). The strain-induced martensitic transformation in Fig. 3(d) and corresponding SADP at Fig. 3(e) at higher magnification further confirms the role of competing fcc and hcp stability with medium SFEs [Fig. 1(a)]. X-ray measurements in Fig. S6 in the Supplemental Material [32] further confirm that the martensite (hcp phase) is not an artifact of the TEM thin-foil effect. Nanosized hcp and fcc lamellas in Fig. 3(f) reveal a composite microstructure acting as a barrier for the dislocation motion, which improved the strain hardening behavior (see Fig. S7 in the Supplemental Material [32]). Recent reports also confirm that simultaneous activation of the twinning-induced plasticity and transformation-induced plasticity effects provides a better strength and ductility combination [78].

The connection between SRO and low-temperature ordering behavior is very important for alloy design [13,79]. Upon cooling, the high-temperature disordered phase gives rise to SRO and ultimately at low temperature to ordering. And, the SRO in the disordered phase is often a "precursor" to the long-range order at low temperatures (or competition between local ordering and clustering). The Warren-Cowley SRO pair-correlations $\alpha_{\mu\nu}^{ss'}(\mathbf{k};T)$ were calculated directly using thermodynamic linear-response theory (for more details, see [13,43,44,56,79–81]). Here, s, s' indices denote sublattices in a crystal structure [1 (2) for fcc (hcp)] and μ, ν denote elements [here 1–4]. For N-component solid solutions, all $\frac{1}{2}N(N-1)$ SRO pair correlations (arising from fluctuations in site-occupation probabilities) are calculated simultaneously [13], similar to that done to get the vibrational stability matrix (i.e., phonon modes and "force constants"). SRO is dictated by pair-interchange energies (chemical stability matrix), i.e., $S_{\mu\nu}^{ss'}(\mathbf{k};T)$ [13,79], the thermodynamically averaged second variation of the free energy with respect to compositional fluctuations [13]. As such, the most unstable SRO mode with wave vector $\mathbf{k}_o$ will have the largest peak in $\alpha_{\mu\nu}^{ss'}(\mathbf{k}_o;T > T_{\text{sp}})$ for a specific μ-ν pair in the solid solution. An absolute instability to $\mathbf{k}_o$ mode [13] occurs below the spinodal temperature T_{sp}, where $[\alpha_{\mu\nu}^{ss'}]^{-1}(\mathbf{k}_o;T_{\text{sp}}) = 0$. If $k_o = (000)$, the alloy is unstable to segregation. Both ordering and clustering peaks may compete. Importantly,

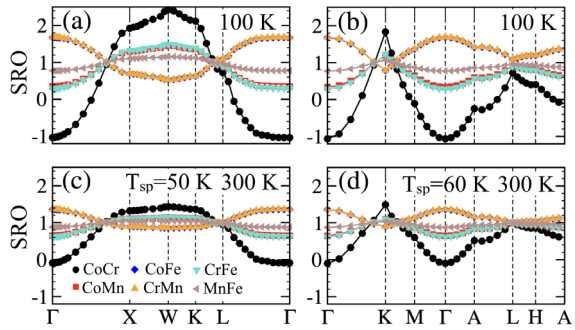

FIG. 4. Warren-Cowley SRO $\alpha^{ss'}_{\mu\nu}(\mathbf{k};T)$ parameters in Laue units for 40 at.%Fe at (a),(b) 100 K and (c),(d) 300 K plotted along fcc (a),(c) and hcp (b),(d) high-symmetry Brillouin zone directions, respectively.

$S^{ss'}_{\mu\nu}(\mathbf{k}_o;T)$ dictates the origin for the SRO, which may be a different pair that peaks in the observable $\alpha^{ss'}_{\mu\nu}(\mathbf{k}_o;T)$, as they are related exactly by an inverse in linear response (see [6,13,44,80]).

For the 40 at.%Fe alloy, the calculated SRO for the fcc and hcp phases is shown in Fig. 4 at 100 K and 300 K (RT). Although SRO at RT is not strong relative to 100 K, it persists over a range of temperatures, which may impact dislocation glide, as found in fcc solid-solution alloys [16]. The spinodal decomposition in solid solutions occurs during, e.g., order-disorder transformation during cooling [82] in which the spinodal temperature indicates the absolute instability to the $\mathbf{k}_o$ mode in SRO [13]. A high mixing entropy keeps solid-solution phases stable at higher temperatures, becoming metastable at low temperatures. To estimate temperature changes on relative stability, we approximate free-energy ΔF[fcc-hcp] by including SRO and electronic entropy as $\Delta F = \Delta E_{\text{form}} - T(\Delta S_{\text{SRO}} + \Delta S_{\text{elec}})$ in the fcc and hcp phases with respect to high-T disorder fcc phase (1500 K having no SRO) with $\Delta F = -1.25$ meV/atom; with a lowering of temperature, ΔF[SRO] $= -2.0$ meV/atom at 1000 K and -8.4 meV/atom at 300 K. Although the energy of fcc lowers relative to hcp, the change is weak. Therefore, no major impact is expected for transition temperature. At low temperatures (with SRO included), the increased stability of fcc over hcp further conforms with the experimentally observed single-phase fcc at 300 K; see Fig. 2(a). The calculated T_{sp} for the fcc and hcp 40 at.%Fe alloy is 50 and 60 K, respectively. So, phase decomposition is not retained at RT, supporting a martensitic transformation as predicted in Fig. 1 and observed in Fig. 3.

Importantly, the state of local chemical SRO is often a precursor to low-temperature order through cooling in most alloys. Notably, the microstructure and local order both can be controlled by composition and/or heat treatment at higher temperatures. To reveal the local chemical order at the onset of dual phase in Fig. 1(a), we analyze the Warren-Cowley SRO parameters $\alpha^{ss'}_{\mu\nu}(\mathbf{k};T)$ that manifest the observable diffuse intensities at 100 K and 300 K for 40 at.%Fe. The diffuse intensities in Figs. 4(a)–4(d) have maximal SRO at W $= (1\,\frac{1}{1}\,0)$ in the fcc phase (indicating $D0_{22}$-type ordering) and at K $= (\frac{2}{3}\,\frac{2}{3}\,0)$ for the hcp phase (indicating $D0_{19}$-type order), which have a possible origin in peaks in $S^{ss'}_{\mu\nu}$ [13] (see Fig. S8 in the Supplemental Material [32], which shows weak temperature dependence). The Co-Cr pair is the most dominant mode that becomes unstable at T_{sp} of 50 K in the fcc phase and 60 K in the hcp phase. The Cr-Mn and Co-Fe pairs contribute with the second most dominant modes with peaks at $\Gamma = (000)$ in the fcc and hcp phases at RT. The presence of SRO at RT, however weak, can impact the dislocation glide [14]. Our bright-field TEM image (Fig. S3 in the Supplemental Material [32]) shows that dislocations pile up at the onset of plastic deformation, indicating strongly localized dislocation structures along a specific (111) plane in fcc alloy. According to Cohen and Fine [83], the first dislocation in the pileup is exposed to higher resistance against slip due to interaction with the favorable (stable) SRO environment, which leads to localized deformation and pileup in $Fe_{40}Mn_{40}Co_{10}Cr_{10}$. All successive dislocations produced by the activated dislocation source and moving along the regions with SRO that was locally destroyed (due to rearrangement of solute) help to overcome the higher resistance, which subsequently helps to nucleate the martensitic phase during deformation. The small $\Delta E^{\text{fcc-hcp}}_{\text{form}}$ poses only a small athermal transformation energy barrier between the fcc and hcp phases that further assists the strain-induced martensitic transformation in Fig. 3. Thus, the dislocation behavior observed (see Fig. S3 in the Supplemental Material [32]) and martensitic transformation shown in Fig. 3 can be associated with the weak SRO, similar to binaries [65,84], as SFE and high yield strength are already known to have a minor effect on the dislocation pileup [16].

Finally, MD simulations were performed (Fig. 5) to understand the deformation mechanism in 40 at.%Fe under uniaxial stress with increasing strain at RT (for method and details, see the Supplemental Material [32]). The microstructure of uniaxially deformed $Fe_xMn_{80-x}Co_{10}Cr_{10}$ at 8% strain (matching experimental conditions) enhanced the ability to form SFs and twins (TWs) with an increase in at.%Fe, as shown in Fig. 5. Our deformation analysis suggests that (see Video S1 in the Supplemental Material [32]) intrinsic fault planes act as a source for twin nucleation. Smallman *et al.* [85] also discussed that lower SFE is preferable for twins as it helps to accommodate large strain; see [86,87]. This mechanism becomes important as, unlike high SFE materials, low SFE alloys cannot develop cross slips that help to absorb large stress. Once the deformation twins are formed, a further increase in strain can either increase TW density or cause existing twins to act as nucleation sites for the hcp, especially at the intersection of SFs and TWs [see Figs. 3(c) and 3(d)].

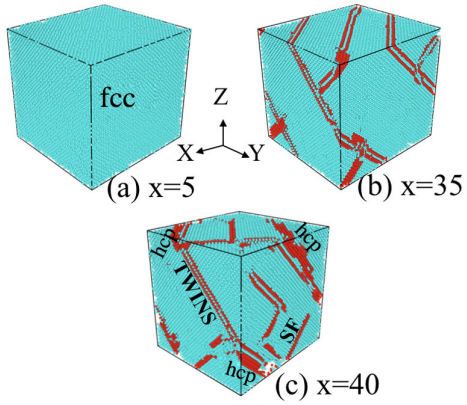

FIG. 5. (a)–(c) Stress-induced martensitic formation from MD under uniaxial (111) loading at 8% strain in $Fe_xMn_{80-x}Co_{10}Cr_{10}$. Twinnability increases with %Fe, with martensite at x = 40 at.%. Mirrored single-layer (red atoms) indicate twin boundaries, and the two hcp layers within the fcc structure (cyan atoms) signify an intrinsic stacking fault (SF).

Shockley partials were found as the primary dislocations during the early loading stage. While Hirth dislocations and stair rods, identified at the later stages, can be responsible for enhancement in strength and ductility due to the formation of a Lomer-Cottrell lock (see Video S1 in the Supplemental Material [32]), which agrees with an extra-stage strain hardening observed in the stress-strain curve for 40 at.%Fe (see Fig. S7 in the Supplemental Material [32]). More details about method and other experimental details are included in the Supplemental Material [32].

In conclusion, using DFT-based Green's function methods in combination with proper configuration averaging using the coherent-potential approximation, we predicted the controlling physics behind the martensitic transformation in a complex $Fe_xMn_{8-x}Co_{10}Cr_{10}$ solid-solution alloy system to occur at the specific composition of x = 40 at.%Fe. We confirmed the theoretical predictions using precision experiments on single-crystal samples. MD simulations support both the DFT prediction and our experimental observation of a martensitic transformation. The tunability of phase energy and stacking-fault energy in HEAs and MEAs using only chemistry and disorder shows the relevance of theory-guided design for the next-generation alloys with superior structure-property correlations, as well as the unique insights for controlling phase transformation in technologically relevant alloys.

Research at Ames Laboratory was supported by the U.S. Department of Energy (DOE), Office of Science, Basic Energy Sciences, Materials Science and Engineering Division. Ames Laboratory is operated by Iowa State University for the U.S. DOE under Contract No. DE-AC02-07CH11358. R. A. acknowledges the support of QNRF under Project No. NPRP11S-1203-170056.

P. S. and S. P. contributed equally to this work.

*Corresponding author.
psingh84@ameslab.gov
†Corresponding author.
ddj@iastate.edu, ddj@ameslab.gov

[1] J.-W. Yeh, S.-K. Chen, S.-J. Lin, J.-Y. Gan, T.-S. Chin, T.-T. Shun, C.-H. Tsau, and S.-Y. Chang, Adv. Eng. Mater. **6**, 299 (2004).
[2] D. Miracle and O. Senkov, Acta Mater. **122**, 448 (2017).
[3] E. P. George, D. Raabe, and R. O. Ritchie, Nat. Rev. Mater. **4**, 515 (2019).
[4] Y. T. Zhu and X. Liao, Nat. Mater. **3**, 351 (2004).
[5] Z. Li, K. G. Pradeep, Y. Deng, D. Raabe, and C. C. Tasan, Nature (London) **534**, 227 (2016).
[6] P. Singh, A. Sharma, A. V. Smirnov, M. S. Diallo, P. K. Ray, G. Balasubramanian, and D. D. Johnson, npj Comput. Mater. **4**, 16 (2018).
[7] Y. Ikeda, I. Tanaka, J. Neugebauer, and F. Körmann, Mater. Charact. **147**, 464 (2019).
[8] S. Picak, J. Liu, C. Hayrettin, W. Nasim, D. Canadinc, K. Xie, Y. Chumlyakov, I. Kireeva, and I. Karaman, Acta Mater. **181**, 555 (2019).
[9] A. Tamm, A. Aabloo, M. Klintenberg, M. Stocks, and A. Caro, Acta Mater. **99**, 307 (2015).
[10] F. X. Zhang, S. Zhao, K. Jin, H. Xue, G. Velisa, H. Bei, R. Huang, J. Y. P. Ko, D. C. Pagan, J. C. Neuefeind, W. J. Weber, and Y. Zhang, Phys. Rev. Lett. **118**, 205501 (2017).
[11] Y. Ma, Q. Wang, C. Li, L. J. Santodonato, M. Feygenson, C. Dong, and P. K. Liaw, Scr. Mater. **144**, 64 (2018).
[12] M. Widom, W. P. Huhn, S. Maiti, and W. Steurer, Metall. Mater. Trans. A **45**, 196 (2014).
[13] P. Singh, A. V. Smirnov, and D. D. Johnson, Phys. Rev. B **91**, 224204 (2015).
[14] J. Ding, Q. Yu, M. Asta, and R. O. Ritchie, Proc. Natl. Acad. Sci. U.S.A. **115**, 8919 (2018).
[15] T. Kostiuchenko, A. V. Ruban, J. Neugebauer, A. Shapeev, and F. Körmann, Phys. Rev. Mater. **4**, 113802 (2020).
[16] R. Zhang, S. Zhao, J. Ding, Y. Chong, T. Jia, C. Ophus, M. Asta, R. O. Ritchie, and A. M. Minor, Nature (London) **581**, 283 (2020).
[17] P. Y. Volosevich, V. Grindnev, and Y. N. Petrov, Phys. Met. Metallogr. **42**, 126 (1976).
[18] Y. Ikeda, I. Tanaka, J. Neugebauer, and F. Körmann, Phys. Rev. Mater. **3**, 113603 (2019).
[19] B. C. D. Cooman, Y. Estrin, and S. K. Kim, Acta Mater. **142**, 283 (2018).
[20] O. Bouaziz, H. Zurob, and M. Huang, Steel Res. Int. **84**, 937 (2013).
[21] D. R. Steinmetz, T. Jpel, B. Wietbrock, P. Eisenlohr, I. Gutierrez-Urrutia, A. Saeed-Akbari, T. Hickel, F. Roters, and D. Raabe, Acta Mater. **61**, 494 (2013).
[22] Z. Wu, H. Bei, G. Pharr, and E. George, Acta Mater. **81**, 428 (2014).
[23] C. Wang, B. Yao, Z. Liu, X. Kong, D. Legut, R. Zhang, and Y. Deng, Int. J. Plast. **131**, 102725 (2020).
[24] B. Uzer, S. Picak, J. Liu, T. Jozaghi, D. Canadinc, I. Karaman, Y. Chumlyakov, and I. Kireeva, Mater. Res. Lett. **6**, 442 (2018).
[25] S. Cotes, M. Sade, and A. F. Guillermet, Metall. Mater. Trans. A **26**, 1957 (1995).

[26] J. He, C. Zhu, D. Zhou, W. Liu, T. Nieh, and Z. Lu, Intermetallics **55**, 9 (2014).
[27] B. Schuh, F. Mendez-Martin, B. Volker, E. George, H. Clemens, R. Pippan, and A. Hohenwarter, Acta Mater. **96**, 258 (2015).
[28] W. Lu, C. H. Liebscher, G. Dehm, D. Raabe, and Z. Li, Adv. Mater. **30**, 1804727 (2018).
[29] Y. Bu, Z. Li, J. Liu, H. Wang, D. Raabe, and W. Yang, Phys. Rev. Lett. **122**, 075502 (2019).
[30] Y. Zhao, T. Yang, Y. Tong, J. Wang, J. Luan, Z. Jiao, D. Chen, Y. Yang, A. Hu, C. Liu, and J.-J. Kai, Acta Mater. **138**, 72 (2017).
[31] T. Yang, Y. L. Zhao, Y. Tong, Z. B. Jiao, J. Wei, J. X. Cai, X. D. Han, D. Chen, A. Hu, J. J. Kai, K. Lu, Y. Liu, and C. T. Liu, Science **362**, 933 (2018).
[32] See Supplemental Material, which includes Refs. [33–53], at http://link.aps.org/supplemental/10.1103/PhysRevLett.127.115704 for supporting results related to discussion in the main text such as methods, mechanical properties (experiments), short-range order (DFT), and deformation analysis (MD).
[33] D. D. Johnson, D. M. Nicholson, F. J. Pinski, B. L. Gyorffy, and G. M. Stocks, Phys. Rev. Lett. **56**, 2088 (1986).
[34] D. D. Johnson and F. J. Pinski, Phys. Rev. B **48**, 11553 (1993).
[35] A. Alam and D. D. Johnson, Phys. Rev. B **80**, 125123 (2009).
[36] A. Alam, B. Kraczek, and D. D. Johnson, Phys. Rev. B **82**, 024435 (2010).
[37] A. Alam and D. D. Johnson, Phys. Rev. B **85**, 144202 (2012).
[38] J. P. Perdew, K. Burke, and M. Ernzerhof, Phys. Rev. Lett. **77**, 3865 (1996).
[39] C. B. Carter and S. M. Holmes, Philos. Mag. A **35**, 1161 (1977).
[40] A. Datta, U. Waghmare, and U. Ramamurty, Scr. Mater. **60**, 124 (2009).
[41] M. Chandran and S. K. Sondhi, J. Appl. Phys. **109**, 103525 (2011).
[42] X.-X. Yu and C.-Y. Wang, Acta Mater. **57**, 5914 (2009).
[43] P. Singh, S. Gupta, S. Thimmaiah, B. Thoeny, P. K. Ray, A. Smirnov, D. D. Johnson, and M. J. Kramer, Acta Mater. **194**, 540 (2020).
[44] P. Singh, A. V. Smirnov, and D. D. Johnson, Phys. Rev. Mater. **2**, 055004 (2018).
[45] A. Sharma, P. Singh, D. D. Johnson, P. K. Liaw, and G. Balasubramanian, Sci. Rep. **6**, 31028 (2016).
[46] J. D. Honeycutt and H. C. Andersen, J. Phys. Chem. **91**, 4950 (1987).
[47] A. Stukowski, Model. Simul. Mater. Sci. Eng. **18**, 015012 (2010).
[48] A. Stukowski and K. Albe, Model. Simul. Mater. Sci. Eng. **18**, 085001 (2010).
[49] J. Li, Q. Fang, B. Liu, Y. Liu, and Y. Liu, RSC Adv. **6**, 76409 (2016).
[50] S. Copley and B. Kear, Acta Metall. **16**, 227 (1968).
[51] I. Karaman, H. Sehitoglu, K. Gall, Y. Chumlyakov, and H. Maier, Acta Mater. **48**, 1345 (2000).
[52] S. Asgari, E. El-Danaf, S. R. Kalidindi, and R. D. Doherty, Metall. Mater. Trans. A **28**, 1781 (1997).
[53] I. Gutierrez-Urrutia and D. Raabe, Acta Mater. **59**, 6449 (2011).
[54] S. Plimpton, J. Comput. Phys. **117**, 1 (1995).
[55] D. Raabe, C. C. Tasan, H. Springer, and M. Bausch, Steel Res. Int. **86**, 1127 (2015).
[56] P. Singh, A. Marshal, A. V. Smirnov, A. Sharma, G. Balasubramanian, K. G. Pradeep, and D. D. Johnson, Phys. Rev. Mater. **3**, 075002 (2019).
[57] M. Gao, J.-W. Yeh, P. Liaw, and Y. Zhang, *High-entropy Alloys: Fundamentals and Applications* (Springer Publishing, New York, 2016).
[58] D. Pierce, J. Jimnez, J. Bentley, D. Raabe, and J. Wittig, Acta Mater. **100**, 178 (2015).
[59] A. Rabinkin, CALPHAD: Comput. Coupling Phase Diagrams Thermochem. **3**, 77 (1979).
[60] P. Kelly, Acta Metall. **13**, 635 (1965).
[61] S. W. Lee and H.-C. Lee, Metall. Mater. Trans. A **24**, 1333 (1993).
[62] R. D. K. Misra, S. Nayak, S. A. Mali, J. S. Shah, M. C. Somani, and L. P. Karjalainen, Metall. Mater. Trans. A **40**, 2498 (2009).
[63] Y. Zhang, Y. Zhuang, A. Hu, J. Kai, and C. Liu, Scr. Mater. **130**, 96 (2017).
[64] A. J. Zaddach, C. Niu, C. C. Koch, and D. L. Irving, JOM **65**, 1780 (2013).
[65] M. B. Kivy and M. A. Zaeem, Scr. Mater. **139**, 83 (2017).
[66] Z. Li, C. C. Tasan, H. Springer, B. Gault, and D. Raabe, Sci. Rep. **7**, 40704 (2017).
[67] S. Huang, H. Huang, W. Li, D. Kim, S. Lu, X. Li, E. Holmström, S. K. Kwon, and L. Vitos, Nat. Commun. **9**, 2381 (2018).
[68] L. Chen, T. Cao, R. Wei, K. Tang, C. Xin, F. Jiang, and J. Sun, Mater. Sci. Eng. **772**, 138661 (2020).
[69] Z. Li, C. C. Tasan, K. G. Pradeep, and D. Raabe, Acta Mater. **131**, 323 (2017).
[70] S. Zhao, G. M. Stocks, and Y. Zhang, Acta Mater. **134**, 334 (2017).
[71] L. Rémy and A. Pineau, Mater. Sci. Eng. **26**, 123 (1976).
[72] Y. Zhang, N. Tao, and K. Lu, Scr. Mater. **60**, 211 (2009).
[73] F. Ebrahimi, Z. Ahmed, and H. Li, Appl. Phys. Lett. **85**, 3749 (2004).
[74] N. I. Medvedeva, D. V. Aken, and J. E. Medvedeva, J. Phys. Condens. Matter **22**, 316002 (2010).
[75] J. Kim, S.-J. Lee, and B. C. D. Cooman, Scr. Mater. **65**, 363 (2011).
[76] K. Jeong, J.-E. Jin, Y.-S. Jung, S. Kang, and Y.-K. Lee, Acta Mater. **61**, 3399 (2013).
[77] Q. Lin, J. Liu, X. An, H. Wang, Y. Zhang, and X. Liao, Mater. Res. Lett. **6**, 236 (2018).
[78] S. Picak, H. Yilmaz, and I. Karaman, Scr. Mater. **202**, 113995 (2021).
[79] P. Singh and D. D. Johnson (to be published).
[80] P. Singh, A. Smirnov, A. Alam, and D. D. Johnson, Acta Mater. **189**, 248 (2020).
[81] D. D. Johnson, in *Characterization of Materials*, edited by E. N. Kaufmann (Wiley, New York, 2012), Ch. 13, pp. 1–31.
[82] J. Zhou, J. Odqvist, J. gren, A. Ruban, M. Thuvander, W. Xiong, G. B. Olson, and P. Hedstrm, Scr. Mater. **98**, 13 (2015).

[83] J. Cohen and M. Fine, J. Phys. Radium **23**, 749 (1962).
[84] V. Gerold and H. Karnthaler, Acta Metall. **37**, 2177 (1989).
[85] R. Smallman and D. Green, Acta Metall. **12**, 145 (1964).
[86] E. Tadmor and N. Bernstein, J. Mech. Phys. Solids **52**, 2507 (2004).
[87] S. Kibey, J. B. Liu, D. D. Johnson, and H. Sehitoglu, Appl. Phys. Lett. **91**, 181916 (2007).